Thermal conductivity of Si and SiGe NWs assessment using atmospheric SthM approach-based analysis – Supplementary Information

Jose Manuel Sojo Gordillo[a], Gerard Gadea Diez[a,d], Mercè Pacios Pujadó[a], Marc Salleras[b], Denise Estrada-Wiese[b], Marc Dolçet[b], Luis Fonseca[b], Alex Morata[a,*], Albert Tarancón[a,c].

[a] Catalonia Institute for Energy Research (IREC), Jardins de Les Dones de Negre 1, 08930, Sant Adrià de Besòs, Barcelona, Spain
[b] Institute of Microelectronics of Barcelona, IMB-CNM (CSIC), C/Til·lers s/n (Campus UAB), 08193, Bellaterra, Barcelona, Spain
[c] Institució Catalana de Recerca I Estudis Avançats (ICREA), Passeig Lluís Companys 23, 08010, Barcelona, Spain
[d – current affiliation] University of Basel, Physics Department, Klingelbergstrasse 82, 4056, Basel
* Corresponding author

1. Tip calibration

Supplementary Figure 1A and B shows SEM images of the Nanothermal probes used in this work. A tip radius of 100 nm was estimated. As it can be seen, the probe consists in a thin film $NiCr/Pd$ resistor which acts both as heater and thermometer. The fabrication process of these kind of tips results in non-negligible oscillation in characteristics among each individual item, with resistance oscillations of about 10% and slightly different thermal behaviour (due to changes in the different layer thicknesses). Therefore, every new tip used needs to be calibrated accordingly prior to its use. On the other hand, once calibrated, these tips are way bulkier than standard topography AFM probes, and each tip used have shown no significance variation after several experiments unless they get damaged somehow.

The probe signal is measured connecting the tip resistor into a Wheatstone bridge (Supplementary Figure 1C) once calibrated. The Wheatstone bridge signal V_{SThM} is linearly proportional to the current I_{Probe} and the tip temperature T_{Probe} (Eq. S. 1) [1].

$$\frac{V_{SThM}}{I_{Probe}} = C_1 \cdot T_{Probe} + C_2 \qquad \text{Eq. S. 1}$$

This way, accordingly to Supplementary Figure 2, tip calibration was done prior to the nanostructure analysis in 4 steps.

i) First, with the tip suspended away from substrate and disconnected of the Wheatstone bridge, an I-V curve was performed over the tip to accurately determine its resistance ($R_{Probe} = V_{applied}/I_{Probe}$) change as a function of the current due to its self/heating (Supplementary Figure 2A). The curve also serves to identify the minimum current in which the self-heating effects starts to take place. This value is crucial in the next steps because of the high difficulty of adjusting the Wheatstone bridge with too small currents. With $R_{probe}(I_{probe})$ curve, the heat dissipated in the tip $\dot{Q}_{Probe}$ can be simply calculated as $\dot{Q}_{Probe} = I_{Probe}^2 R_{Probe}$.

ii) Secondly, the tip is connected to the Wheatstone bridge and with a current unable to produce self/heating the bridge is equilibrated, i.e. the variable resistor is changed until V_{SThM} is set to 0. A value of I_{Probe} = 0.1 mA was determined to be a good trade-off between high enough current for a precise V_{SThM} measurement and still unable to produce self-heating.

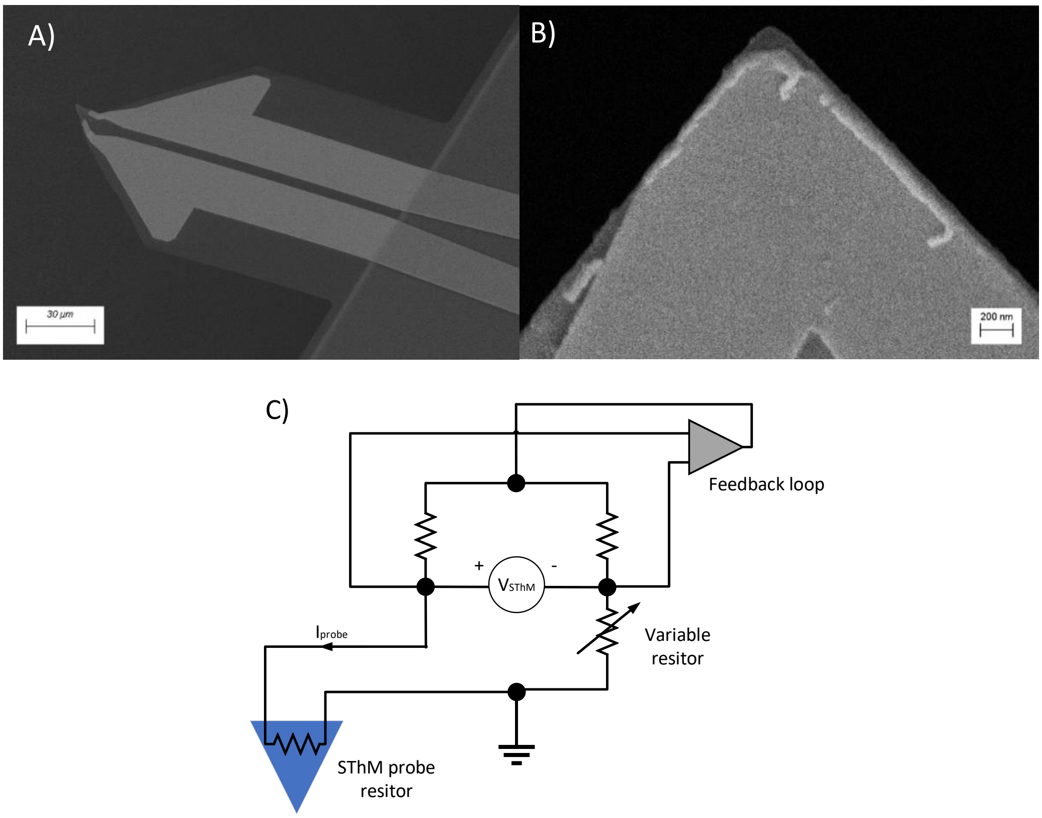

Supplementary Figure 1. A) SEM image of the SiO2 – Pd SThM NanoThermal probe used. B) Inset of the probe tip, the tip radius was calculated to be $\sim 100\ nm$. C) Schematics of the Wheatstone bridge employed to control the current set into the SThM resistor I_{probe}.

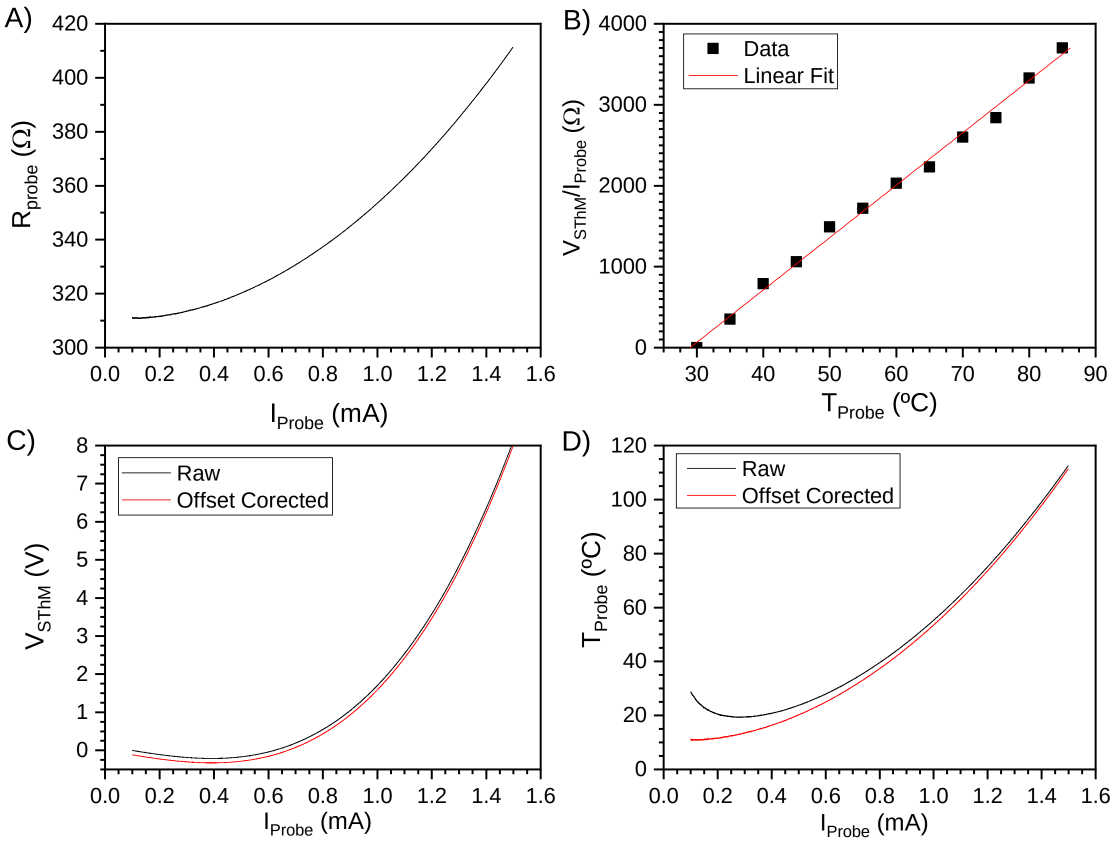

Supplementary Figure 2. A) Resistance of the tip resistor as a function of the forced current imposed when performing an I-V curve. B) $\boldsymbol{V_{SThM}/I_{Probe}}$ as a function of the tip temperature for $\boldsymbol{I_{Probe}}$ set to $\mathbf{0.1}\ \boldsymbol{mA}$ C) $\boldsymbol{V_{SThM}}$ as a function of $\boldsymbol{I_{Probe}}$ in air (far away from sample) D) Temperature as a function of

$\boldsymbol{I_{Probe}}$ calibration curve obtained by combinining B) and C). For $\boldsymbol{I_{Probe} < 0.5\, mA}$ the error is important.

iii) Then, with the tip connected to the Wheatstone bridge, the values of constants C_1 and C_2 of Eq. S. 1 were calibrated by putting the tip in contact with a heater at known temperature (Park's Universal Liquid Cell temperature controller) and making several measurements of V_{SThM} at fixed I_{Probe} (Supplementary Figure 2B). Again, a value of I_{Probe} = 0.1 mA was used.

iv) Later, a self-heating curve with the tip connected to the Wheatstone bridge was performed by forcing I_{Probe} up to 1.6 mA, enough to produce noticeable changes in tip resistance (Supplementary Figure 2C). This curve allows to relate the tip resistance change due to the self-heating directly with the whetstone bridge voltage V_{SThM}. Removing the offset V_{SThM} voltage at $I_{Probe} = 0$ helps removing artefacts produced by the division of a finite quantity by zero at low currents. However, it is worth noticing how the V_{SThM} might still slightly vary as current changes due to a non-perfect variable resistor adjustment in step ii) at such low currents (in absence of self-heating). Yet, it is quickly masked by the self-heating contribution ($I_{Probe} > 0.8\, mA$) where the measurements take place.

v) Finally, combining the values of K_1 and K_2 found in Supplementary Figure 2B with the V_{SThM} signal as a function of I_{Probe} shown at Supplementary Figure 2C, a relationship between the tip temperature T as a function of I_{Probe} can be obtained. The result is presented at Supplementary Figure 2D, which leads to straight calculation of $\Delta T = T_{Probe} - T_\infty$ (with T_∞ being 25 °C). Again, an artefact of temperature changes at lower I_{Probe} might appear as a consequence of the non-perfect variable resistor adjustment but the effects becomes negligible with the self-heating contribution ($I_{Probe} > 0.8\, mA$).

2. Conductance step extraction from the current curve:

Supplementary Figure 3 shows a raw current and force curve versus tip height used to derive the conductance change in the tip using the expression $G = \dot{Q}_{Probe}/\Delta T = ({I_{Probe}}^2 R_{Probe})/\Delta T$. The force curve inflexion point is then used to offset the tip position curve to $z = 0$ at this specific point. Once G is calculated as a function of the corrected tip position, a stepwise polynomial fit before and after the contact jump at $z = 0$ allows to easily fit δG.

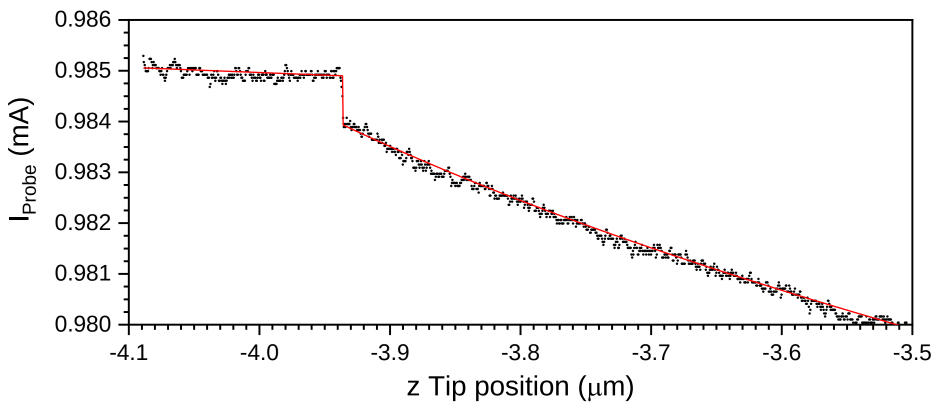

Supplementary Figure 3. Raw current curve as a function of the tip position (dots) used to compute the tip conductance as $G = \dot{Q}_{Probe}/\Delta T = ({I_{Probe}}^2 R_{Probe})/\Delta T$. The red line represents the result of a stepwise polynomial fit used to compute δG.

It is worth noticing that since G and δG measurements are derived from another measured variables (current and temperatures). Specifically, ambient temperature stability is of major importance to ensure a proper assessment of ΔT and subsequently of G. Therefore, measurements should be performed in a properly isolated room with no temperature fluctuations. Moreover, it is recommended to actively stabilize the substrate temperature in order to better ensure this issue. A Peltier module as the one used in this work (see experimental section) would be desirable, as it can properly compensate for both increasing or decreasing small ambient temperature fluctuations in the surrounding of the microscope.

3. Validation of assumptions:

During the description of the problem, some strong assumptions neglecting terms of the complete system thermal model has been made. This section aims to validate such assumptions and the applicability of Eq. 1 of the article, copied here for brevity:

$$\delta G = G_{(post)} - G_{(pre)} = \frac{1}{R_C + R_{NS}(y)} \qquad \text{Eq. 1}$$

3.1. Full contact model including meniscus and solid-air contact conductance terms:

Supplementary Figure 4 top row - i.e. A), B) and C) - schematizes the conductances that would participate in the total tip conductance $G \equiv \dot{Q}_{Probe}/\Delta T$ if the measurement was performed in vacuum, in which only solid conduction takes place. Supplementary Figure 4 bottom row - i.e. D), E) and F) - includes additional terms that are present in atmospheric conditions. Supplementary Figure 4 E) and F) includes additional thermal paths in series/parallel with the ones present in the vacuum scheme, which were omitted in the simplified version shown at the body of the article for the sake of clarity.

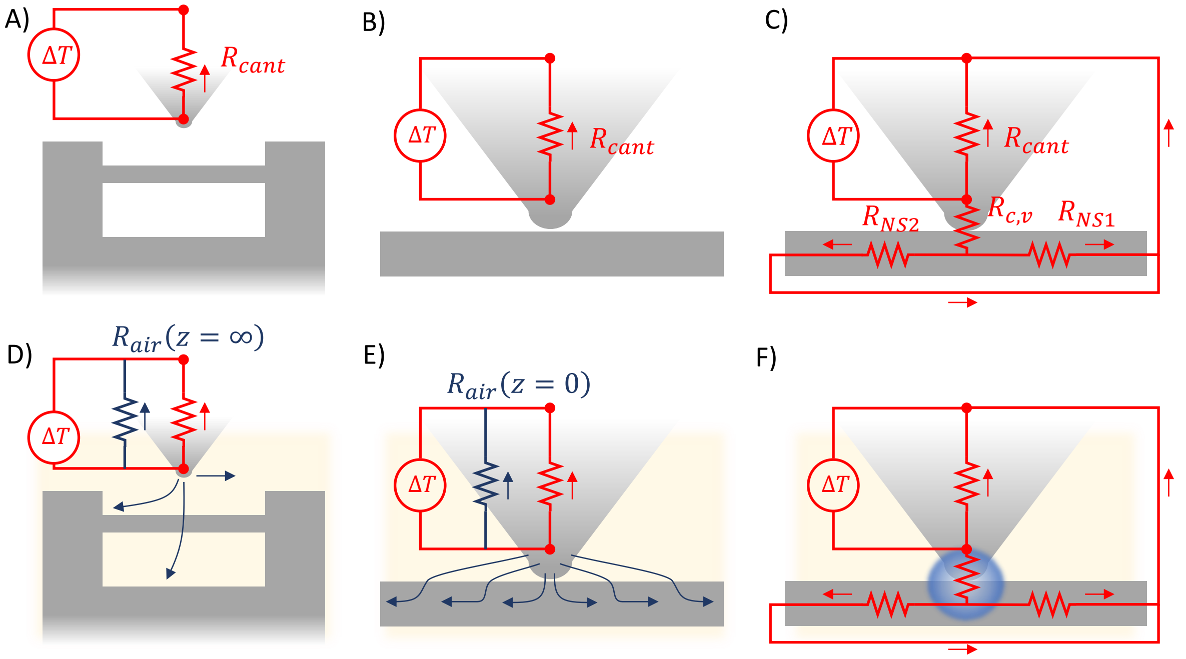

Supplementary Figure 4. Detailed schemes of the equivalent thermal circuits of the system in vacuum A) - C) and air D) - F). First images A) and D) shows the circuit when the tip is away from the sample. Only cantilever loses are present in the case of vacuum (A). In air, conduction loses to air also take place, and will increase as z decreases since the probe-substrate distance is reduced. Second images B) and E) show the circuit immediately before the contact event. There are no changes in the vacuum scheme (B), however, for the case of air (E), a finite amount of heat flows through the air gap between tip and NS. Finally, after the contact C) and E) the NS conductance and contact resistances are added in parallel. In the case of air (E), a meniscus might be formed, creating a parallel path for heat evacuation to towards the NS.

First, just before the tip contacting the NS, the air gap between tip and the underlying portion of NS is very small leading to a very high conductance through air, termed R_{SAS} in the scheme. If one were to consider only Fourier's law for the determination, R_{SAS} would trend to 0, because the gap just before contacting is virtually null. However, in a real experiment the solid (tip) – air (gap) – solid (NS) contact thermal resistance exists, hence the nomenclature "SAS". It is mostly related to the scattering effect of gas molecules in the two surfaces. Therefore, $R_{SAS} = 1/G_{SAS}$ has a finite value that enables the path through the NS already before contact whose relevance depends on its relative magnitude.

On the other hand, and as already introduced in the article, after contact a water meniscus is formed. In this way, the tip-NS contact conductance can be split into two parallel contributions, related to direct solid-solid contact ($G_{SS} = 1/R_{SS}$) and to the water meniscus ($G_W = 1/R_W$). Any remaining contribution from the air can be neglected because: (i) the droplet is in the region of the former small gap occupying the former G_{SAS} channel; and (ii): the rest of possible parallel paths through air to the NS are already at distance larger than the mean free path and subject to scattering events, leading to a decreased conductance.

The magnitudes of G_{ss} and G_w contact conductances have been estimated only for flat substrates and are both in the range 0.1 – 0.2 µW/K [2,3]. In the case of contacting a small size object as NW – or an even smaller rough appendix of a NW – one might expect the direct solid-solid conductance decrease, as $G_{SS} \propto$ contact area. However, the size of the meniscus (on the order of 50 – 100 nm [4]) is not expected to decrease. The value of G_W might increase instead as the droplet might end up surrounding the whole NS – and contacting all the outer rough structures, if present – leading to an increased contact area. Thus, independently of the relative weight of each conductance, the combined contact conductance after contact G_C is at least $0.1\ \mu\mathrm{W/K}$ (or equivalently $R_C < 10\ \mathrm{K}/\mu\mathrm{W}$).

Hence, one can re-write Eq. 1 with the conductances of the system before and after the contact (Eq. S. 2 and Eq. S. 3 respectively) more rigorously including all terms as:

$$\frac{1}{R_{pre}} = G_{pre} = \frac{1}{R_{SAS} + R_{NS}} + \frac{1}{R_{tip}} + \frac{1}{R_\infty} \qquad \text{Eq. S. 2}$$

$$\frac{1}{R_{post}} = G_{pre} = \frac{1}{R_C + R_{NS}} + \frac{1}{R_{tip}} + \frac{1}{R_\infty} \qquad \text{Eq. S. 3}$$

In this way, the conductance change produced in the contact event can be expressed as the difference between the previously defined conductances:

$$\frac{1}{R_{post}} - \frac{1}{R_{pre}} = \delta G_s = \frac{1}{R_C + R_{NS}} - \frac{1}{R_{SAS} + R_{NS}} \qquad \text{Eq. S. 4}$$

$$\delta G_s = \frac{R_{SAS} - R_C}{R_{NS}^2 + R_{NS}(R_C + R_{SAS}) + \left(\frac{1}{R_C} + \frac{1}{R_{SAS}}\right)^{-1} R_{SAS}} \qquad \text{Eq. S. 5}$$

3.2. Effects of extra terms for the validity of the assumption:

Eq. 1 above – central for the method proposed in the article – is making use of the implicit assumption $R_C \sim R_{NS} \ll R_{SAS}$, and then the contact resistance effectively substitutes R_{SAS} since $G_C + R_{SAS} \cong G_C$. If we simplify Eq. S. 5 with this assumption, we get the expression used in Eq. 5.

$$\delta G_s \cong \frac{R_{SAS} - R_C}{R_{NS}^2 + R_{NS}(R_C + R_{SAS}) + R_C R_{SAS}} \cong \frac{R_{NC}}{R_{NS} R_{SAS} + R_C R_{SAS}} \cong \frac{1}{R_{NS} + R_C} \qquad \text{Eq. S. 6}$$

In this way, an assumed R_{NS} is deduced from a δG_s under this approximation:

$$R_{NS}^{Assum} = \frac{1}{\delta G_s} - R_C \qquad \text{Eq. S. 7}$$

However, in order to assess whether or not this assumption ($R_C \sim R_{NS} \ll R_{SAS}$) is valid, the value of R_{SAS} must be estimated and used to verify that the ratio R_{SAS}/R_C obtained in this work is high enough to hold the approximations. If the simple vacuum R_{NS} model is used (Eq. 3 i.e. when $h = 0$), the R_{NS} can be described as:

$$R_{NS}(y) = f(y)R_0 = f(y)\frac{L}{\kappa A_C} \qquad \text{Eq. S. 8}$$

Where $f(y) = [1/4 - (y/L)^2]$. Thus, from the values of R_{SAS}, R_C and the intrinsic properties of the NS (R_0), the real δG_s values that would ideally be measured can be estimated at a position x.

$$\delta G_s(y) = \frac{R_{SAS} - R_C}{(f(y)R_0)^2 + (f(y)R_0)(R_C + R_{SAS}) + R_C R_{SAS}} \qquad \text{Eq. S. 9}$$

On the other hand, if a conductance change δG_s is measured at the position x, a thermal conductivity will be inferred with certain error if Eq. S. 6 is used instead of using the full model (Eq. S. 5).

$$\kappa_{inf} = f(y)\frac{L}{R_{NS}^{Assumed} A_C} = f(y)\frac{L}{\left(\frac{1}{\delta G_s} - R_C\right)A_C} = f(x)\frac{R_0^{Real}\,\kappa_{Real}}{\left(\frac{1}{\delta G_s} - R_C\right)} \qquad \text{Eq. S. 10}$$

The error committed in the evaluating of the thermal conductivity κ_{inf} can be assessed with the ratio $\kappa_{Infer}/\kappa_{Real}$ (Eq. S. 11). This can be studied as a function of the real conductance changes which can subsequently be deduced using Eq. S. 9 as a function of the ratio R_{SAS}/R_C and the intrinsic properties of the NS.

$$\frac{\kappa^{Real}}{\kappa^{Infer}} = \frac{f(y)R_0^{Real}}{\left(\frac{1}{\delta G_s(y)} - R_C\right)} \qquad \text{Eq. S. 11}$$

Supplementary Figure 5 shows the evolution of this ratio, using a reasonable value of R_C of 4.6 $K/\mu W$; $\kappa_{Real} = 20\ W/m\cdot K$; $L = 10\ \mu m$ and $\phi = 100\ nm$. As it can be appreciated, the assumption starts to be valid for ratios higher than 10^2 - 10^3.

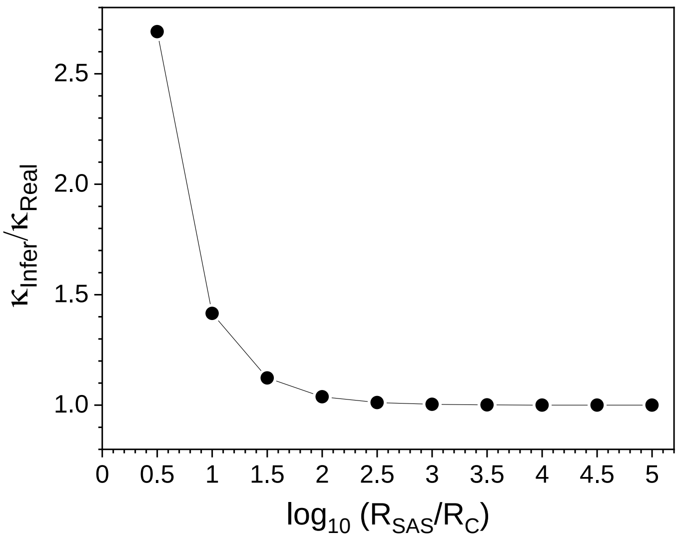

Supplementary Figure 5. Ratio of the inferred thermal conductivity respect to the real one when using the assumption $\boldsymbol{R_C \sim R_{NS} \ll R_{SAS}}$ as a function of the ratio between the non-contact resistance $\boldsymbol{R_{SAS}}$ and the contact resistance $\boldsymbol{R_C}$ in logarithmic scale at $\boldsymbol{y = 0}$.

By following the work of Giri [5], in the case of air as transfer fluid, assuming no influence of the solid (because of its relatively high thermal conductivity compared with air) and a tip radius of 50 nm, a value for R_{SAS} immediately before the contact of ~530 $K/\mu W$ is evaluated. Since $R_c < 10$ K/μW then the ratio $R_{SAS}/R_C > 50$. Thus, according to Supplementary Figure 5, a ratio of $\kappa_{Infer}/\kappa_{Real} = 0.97$ is obtained, confirming the validity of our assumption.

4. Thermal resistance nanostructure model:

4.1. Temperature profile along a 1D nanostructure segment:

As commented in Section 3.2., the temperature profile along the NS is derived from the solution of the heat equation with the specific boundary conditions of the problem. This section aims to clarify the process.

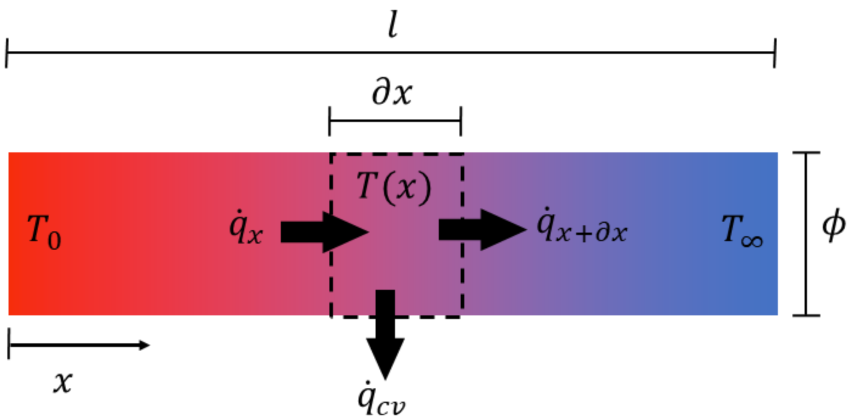

Supplementary Figure 6. Schematic of the differential NS section considered.

Let's consider a differential section of NS in steady state $\left(\frac{\partial T}{\partial t} = 0\right)$ where there is conduction along the circular cross section ($S_x(x) = \frac{\pi}{4}\phi(x)^2$) and convection cooling through the differential area exposed to air ($dS_{cv}(x) = \pi\phi(x)dx$) as shown in Supplementary Figure 6. A heat flow balance leads to:

$$-\frac{\partial \dot{q}_\kappa(x)}{\partial x} = \frac{\partial \dot{q}_{cv}(x)}{\partial x} \qquad \text{Eq. S. 12}$$

The conduction heat $\dot{q}_\kappa(x)$ is defined using Fourier's law. Assuming a constant diameter along the NS:

$$\dot{q}_\kappa(x) = -\kappa(x)\, S_x(x)\frac{\partial T(x)}{\partial x} = -\kappa\,\pi\frac{\phi^2}{4}\frac{\partial T(x)}{\partial x} \qquad \text{Eq. S. 13}$$

The cooling term is defined using Newton's cooling law. Assuming constant convective coefficient h and constant section along the NSs:

$$\frac{\partial \dot{q}_{cv}(x)}{\partial x} = h\, dS_{cv}(x)(T(x) - T_\infty) = h\,\pi\phi\,(T(x) - T_\infty) \qquad \text{Eq. S. 14}$$

Substituting in Eq. S. 12 and rearranging terms, the ordinary differential equation (ODE) of the model is set:

$$\kappa\,\pi\frac{\phi^2}{4}\left(\frac{\partial^2 T(x)}{\partial x^2}\right) = h\,\pi\phi\,(T(x) - T_\infty) \qquad \text{Eq. S. 15}$$

$$\left(\frac{\partial^2 T(x)}{\partial x^2}\right) - \frac{4\,h}{\kappa\,\phi}\,(T(x) - T_\infty) = 0 \qquad \text{Eq. S. 16}$$

Here a double variable change to m and θ eases the solution of the differential equation:

$$\frac{\partial^2 \theta(x)}{\partial x^2} - m^2\theta(x) = 0 \qquad \begin{cases} \theta(x) = T(x) - T_\infty \\ m^2 = \dfrac{4\,h}{\kappa\,\phi} \end{cases} \qquad \text{Eq. S. 17}$$

The generic solution of the ODE is of the form $\theta(x) = C_1 e^{-mx} - C_2 e^{mx}$ therefore two boundary conditions are needed to define the specific solution:

a. At the SThM tip position, the temperature is defined as T_0.
b. The temperature at the NS end is equal to the bulk, which is assumed to be in thermal equilibrium with the ambient air.

Thus:

$$\begin{cases} T(x=0) = T_0 \\ T(x=l) = T_\infty \end{cases} \rightarrow \begin{cases} \theta(x=0) = T_0 - T_\infty = \theta_0 \\ \theta(x=l) = T_\infty - T_\infty = 0 \end{cases} \qquad \text{Eq. S. 18}$$

Substituting into the general solution leads to the following terms for both constants:

$$C_1 = \frac{T_0 e^{2ml}}{e^{2ml} - 1} \qquad C_2 = -\frac{T_0 e^{2ml}}{e^{2ml} - 1} \qquad \text{Eq. S. 19}$$

Introducing the constant values in the general solution yields the following expression.

$$\theta(x) = \frac{\theta_0 e^{-mx}}{e^{2ml} - 1}\left(e^{2ml} - e^{2mx}\right) \qquad \text{Eq. S. 20}$$

Alternatively, the expression can be written as a function of the temperature and the tip position y where the the $\pm$ sign is selected depending the section (left or right chosen):

$$T(x) = \frac{(T_0 - T_\infty)e^{-mx}}{e^{2m\left(\frac{L}{2}\pm y\right)} - 1}\left(e^{2m\left(\frac{L}{2}\pm y\right)} - e^{2mx}\right) \qquad \text{Eq. S. 21}$$

As it can be seen in its dimensionless representation of Supplementary Figure 7 when $\kappa = 15\ W/mK$ and $\phi = 90\ nm$ and $L = 8.9\ \mu m$ and h ranges from 0 to 10 kW/m^2K. When the product $mL \rightarrow 0$ the exponential functions $e^x \rightarrow 1 + x$ (Taylor expansion near 0) and thus after applying the limit, Eq. S. 20 reduces to the linear profile expected for conduction through a non-cooled solid (termed as “only conduction” in the plots).

$$T(x) = \frac{(T_0 - T_\infty)(1 - mx)}{(1 + 2mL - 1)}(1 + 2ml - 1 - 2mx) = \left(1 - \frac{x}{L}\right)(T_0 - T_\infty) \qquad \text{Eq. S. 22}$$

For values of the mL product lower than 0.5 the fully conduction approximation is completely valid.

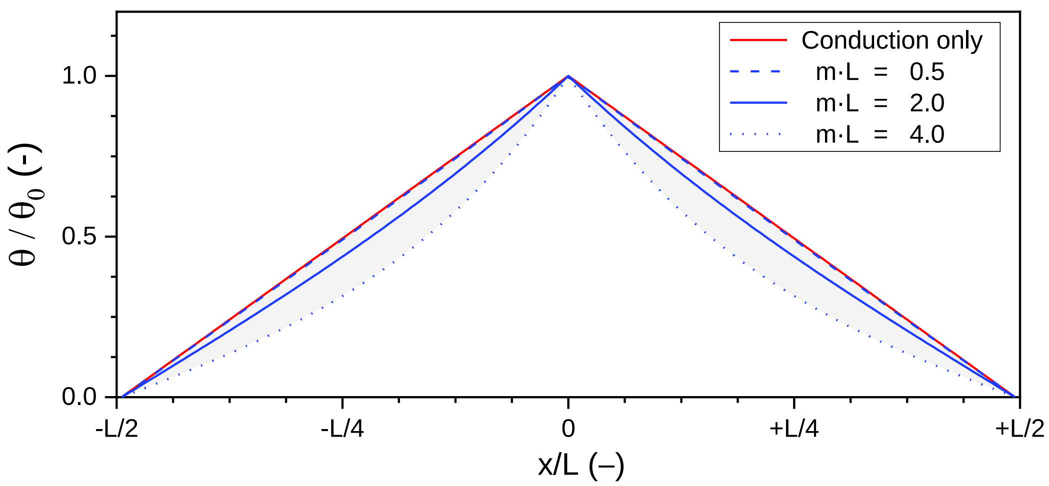

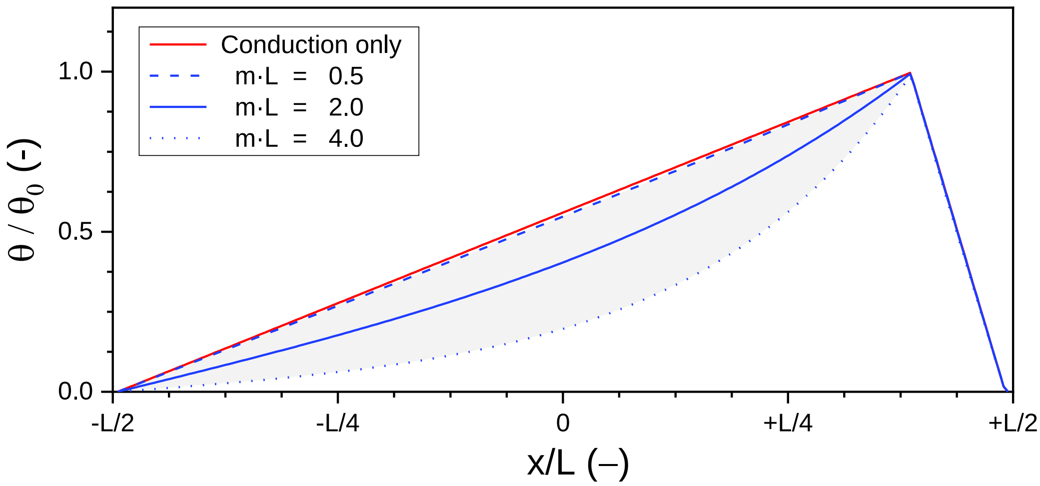

Supplementary Figure 7. Temperature profiles as a function of the longitudinal axis several combinations of $m \cdot L$. A) SThM tip cantered ($y = 0$). B) Tip at $y = 3/8\, L$.

4.2. 1D NS thermal resistance:

The heat flowing from the tip to a segment of air-cooled NS can be obtained using Fourier's law at the boundary $x = 0$.

$$\dot{q}(x=0) = -\kappa \frac{\pi\phi^2}{4} \frac{\partial T(x)}{\partial x}\bigg|_{x=0} = -\kappa \frac{\pi\phi^2}{4} \frac{\partial \theta(x)}{\partial x}\bigg|_{x=0} \qquad \text{Eq. S. 23}$$

Derivating Eq. S. 20 and assessing at $x = 0$:

$$\frac{\partial \theta(x)}{\partial x}\bigg|_{x=0} = \left[\frac{m\theta_0 e^{-mx}}{1-e^{2ml_i}}\left(e^{2ml_i} - e^{2mx}\right) + \frac{2m\theta_0 e^{mx}}{1-e^{2ml_i}}\right]_{x=0} = \theta_0 m \left[\frac{2}{1-e^{2ml_i}} - 1\right] \qquad \text{Eq. S. 24}$$

Using the last two equations one can obtain the heat that flows and conductance from the tip (at T_0) to a segment of air-cooled NS of length l_i connected to the heat sink (at T_∞), with $\theta_0 = T_0 - T_\infty$, provided that the bulk-NS contact thermal resistance is negligible. For the NW considered in this work, our previous studies have shown that the epitaxial growth allows such assumption (see experimental section 5 in the main article). Other top-down approaches such as metal assisted chemical etching (MACE) [6–9] or lithography [10–13] are suited for this assumption as well. Therefore, the expression remains:

$$\dot{Q}_{NS}^{l_i} = -\kappa \frac{\pi\phi^2}{4} m\theta_0 \left[\frac{2}{1-e^{2ml_i}} - 1\right] = G_{NW}^{l_i}\theta_0 \qquad \text{Eq. S. 25}$$

The total heat flowing from the tip trough the NS is obtained by considering the contributions of both branches (left with l_L and right with l_R, see Figure 2 in the main article):

$$\dot{Q}_{NS} = \dot{Q}_{NS}^{l_L} + \dot{Q}_{NS}^{l_R} = \theta_0\left[G_{NS}^{l_L} + G_{NS}^{l_R}\right] \qquad \text{Eq. S. 26}$$

$$\dot{Q}_{NS} = \kappa \frac{\pi\phi^2}{4} 2m \left[1 - \frac{1}{1-e^{2ml_1}} - \frac{1}{1-e^{2ml_2}}\right]\theta_0 \qquad \text{Eq. S. 27}$$

Or alternatively it can be expressed as a function of the tip position y, since $l_1 = L/2 - y$ and $l_2 = L/2 + y$.

$$\dot{Q}_{NS} = \kappa \frac{\pi\phi^2}{4} 2m \left(1 - \frac{1}{1-e^{m\left(L-\frac{y}{2}\right)}} - \frac{1}{1-e^{m\left(L+\frac{y}{2}\right)}}\right)\theta_0 \qquad \text{Eq. S. 28}$$

The thermal conductance G and thermal resistance $R = \theta_0/\dot{Q}_{NS}$ are readily obtained from Eq. S. 28.

$$G = \kappa \frac{\pi\phi^2}{4} 2m \left(1 - \frac{1}{1 - e^{m\left(L - \frac{y}{2}\right)}} - \frac{1}{1 - e^{m\left(L + \frac{y}{2}\right)}}\right) \quad \text{Eq. S22}$$

$$R = \frac{4L}{\pi\phi^2\kappa} \times \left\{2mL \left(1 - \frac{1}{1 - e^{2m\left(L - \frac{y}{2}\right)}} - \frac{1}{1 - e^{m\left(L + \frac{y}{2}\right)}}\right)\right\}^{-1} \quad \text{Eq. S23}$$

Analogously to the procedure employed in Supplementary section 4.1, when there is no air-cooling ($h \rightarrow 0$) one can expand the exponentials e^x to $1 + x$ and take the limit $mL \rightarrow 0$, which will simplify the term in brackets in Eq. S. 2, leading to:

$$R_{vac} = \frac{4L}{\pi\phi^2\kappa} \times \left[\frac{1}{4} - \left(\frac{y}{L}\right)^2\right] \quad \text{Eq. S24}$$

Supplementary Figure 8 shows an example of the profiles of R. Higher values of h leads to flatter profiles. For L product values lower than 0.5, the approximation of Eq. S. 3 (termed as "only conduction" in the plot) is valid.

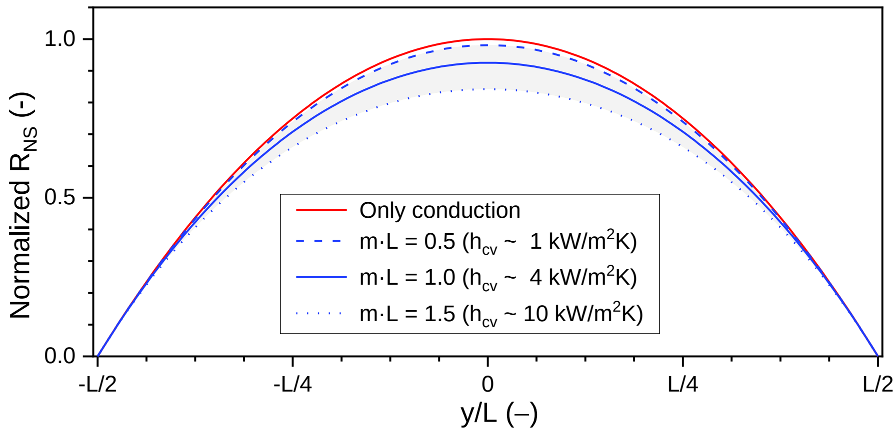

Supplementary Figure 8. Estimation of a NS thermal resistance longitudinal profile as a function of the SThM tip position and the mL product for $\kappa = 15\ W/mK$ and $\phi = 90\ nm$ and $L = 8.9\ \mu m$.

5. The effective convection term:

As discussed in the theoretical discussion (Section 3.3), an estimation of the air losses h provides a tool to improve the accuracy of the fitting model and enables the use of Eq. 6 instead of Eq. 5.

5.1. Identification of the underlying physical modeling:

The dimensionless Rayleigh number Ra defines the ratio between buoyancy forces and viscous forces [14]. For a given characteristic length L_c and a temperature difference ΔT between the solid surface and the environment, a $Ra < 10$ indicates that the viscous forces are dominant and heat transfer can be modelled as a diffusion problem. At the scale of or problem L_c, which in this case can be considered as the equivalent NS diameter ϕ , a Ra of $\sim 10^{-12}$ is obtained. Thus, no convection is expected no matter the imposed temperature gradient, the NS length nor the NS equivalent diameter in the ranges of operation of the problem ($\Delta T \in [10 - 100]\ K, L_c \in [500 - 5000]\ nm$ and $\phi \in [50 - 200]\ nm$ respectively).

However, due to the small scale of the problem, the conduction modelling via diffusion equations is not valid too close of the NS walls either, since ϕ and the distance from the NS to the substrate are not distinctly above the mean free path of the cooling medium (λ_{air}= 63 nm [15]). Indeed, the dimensionless Knudsen number $Kn = \lambda/l$, defined as the ratio of the molecular mean free path length to a representative physical length scale [16], ranges from 1 to 0.05 depending on the characteristic length L_c considered for its calculation. In this situation one cannot adopt a purely diffusive model (Fourier's law) for obtaining h (e.g. as the shape factors of [14]). Thus, free molecular flow needs to be modelled in the surrounding of the NSs surfaces to accurately model the air heat transfer loses.

5.2. The two-layer model:

A two-layer model represented in Supplementary Figure 9 is employed to model the effective convective term. According to Wang et al. [17], in this model the equivalent Nusselt number of the heat transfer problem can be computed as follows:

$$Nu = \frac{4\,\alpha_f f_{ncr}\xi/\pi}{\beta + f_{ncr}(\xi+\Psi)\ln\left(\frac{n_r(\xi+0.4)}{\xi+\Psi}\right)} = 2r_{NS}\frac{h}{\kappa_{air}} \qquad \text{Eq. S. 29}$$

Where α_f is the gas accommodation factor for the solid material surface $\xi = r_s/\lambda = r_{NW}/\lambda = Kn^{-1}$ is the normalized solid (NS) radius which is indeed the inverse of the Knudsen number of the problem, being λ the mean molecular free path, $\Psi = \Delta/\lambda$ is the normalized non-continuum layer thickness, n_r is the ratio of the continuous radius layer with respect to 1.4 times the surface radius, β is a geometrical correction factor (equal to $1/24$ for a cylinder) and f_{ncr} a correction factor of the molecular impact flux.

The mean free path is calculated as:

$$\lambda = \frac{K_b T}{\sqrt{2}\,\pi\, d_m^2\, P} \qquad \text{Eq. S. 30}$$

Being K_b the Boltzmann constant, T the temperature, d_m the molecular diameter (for the case of air, N_2 molecule diameter is used) and P the gas pressure. Finally, the molecular impact flux correction factor is expressed as:

$$f_{ncr} = \xi\left(1 + \xi e^{\xi}\, Ei(-\xi)\right) \qquad \text{Eq. S. 31}$$

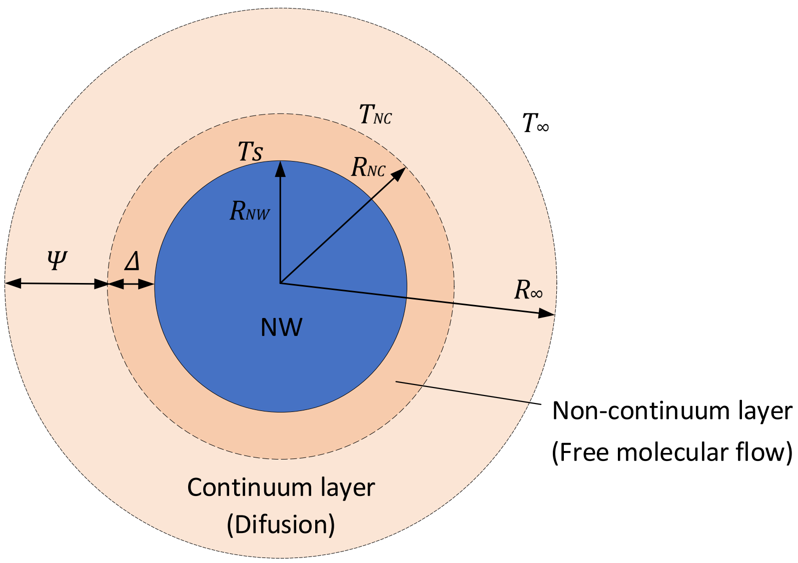

Supplementary Figure 9. Two-layer model scheme applied to a circular nanowire. The inner layer (non-continuum) is modelled using a free molecular regime whereas the outer layer (continuum) is solved using diffusion approach. Adapted from [17].

Where $Ei(x)$ stands for the exponential integral of x. Supplementary Table 1 summarizes the values used in this work for all parameters of the aforementioned model and its sources.

Supplementary Table 1. Summary of parameters used for h estimation using the 2-layer model.

Parameter	Expression	Value	Ref
λ	$\frac{K_b T}{\sqrt{2}\,\pi\, d_m^2\, P}$	100 nm	[18]
d_m	$d_m(Gas)^*$	308 pm	[19]
Δ	$\lambda/0.05^{\dagger}$	2 µm	[18]
ξ	r_{NW}/λ	1	[17]
Ψ	Δ/λ	20	[18]
n_r	$r_\infty/(1.4\, r_{NW})$	100	[17]
α_f	$\alpha_f(Gas, Solid)^*$	0.83	[20]
β	$\frac{1}{8}\int_0^{2\lambda} \frac{\sigma_{NW}}{\sigma_g} dx$	$\frac{1}{24}$	[17]
f_{ncr}	$\xi\left(1 + \xi e^{\xi}\, Ei(-\xi)\right)$	1	[17]

* *Experimental values*

† *Forced to have Kn < 0.05 in the transition to continuum media*

5.3. Estimations of the effective heat transfer coefficient:

Supplementary Figure 10 shows the predicted Nusselt number and corresponding heat transfer coefficient of the described two-layer model. The shadowed regions represent the expected range for the problem conditions, i.e. an $\sim$100 kPa and NW diameters ranging from 50 to 250 nm. As it can be appreciated, the heat transfer coefficient is calculated to be in the 2 - 8 kW/m^2K range.

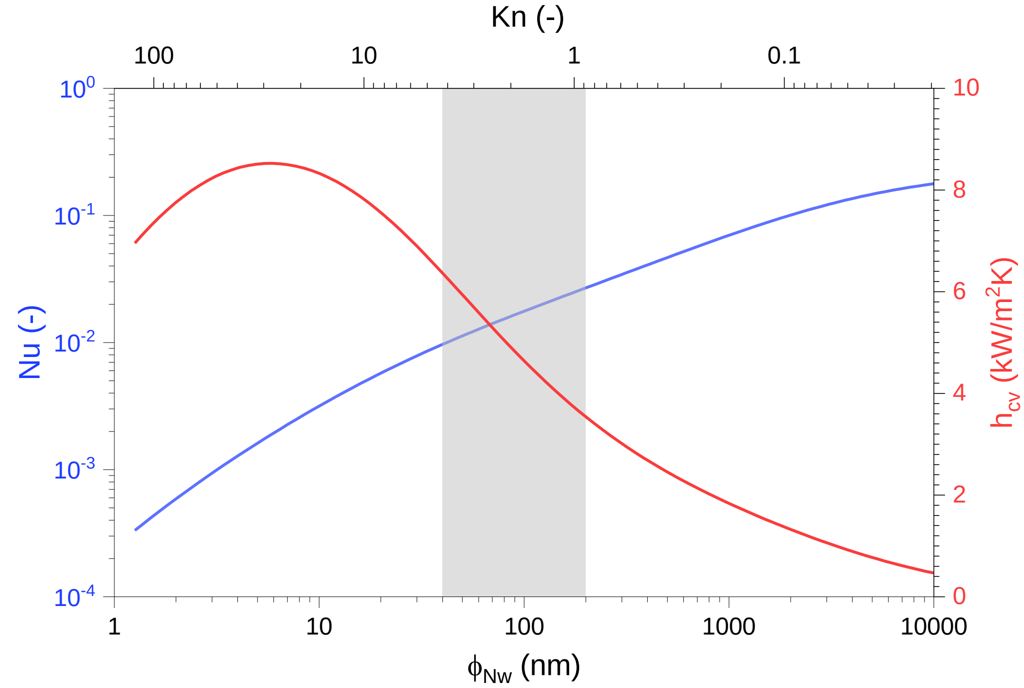

Supplementary Figure 10. Estimation of the Nusselt number $\boldsymbol{Nu}$ and the heat transfer coefficient $\boldsymbol{h}$ as a function of NW diameter. Top $\boldsymbol{x}$ axis represents the equivalent Knudsen number $\boldsymbol{Kn}$ for that particular conditions.

6. SiGe Composition:

The micromachined device used to growth suspended Si and SiGe NWs is mainly made of Si, thus making impossible to compositionally characterize the scanned SiGe NW due to the strong Si signal of the background. In order to overcome this issue, an EDX analysis (Supplementary Figure 11A) was performed over vertical SiGe NWs grown over Si substrate under the same CVD process (Supplementary Figure 11B). A Ge composition of x = 0.33 was estimated.

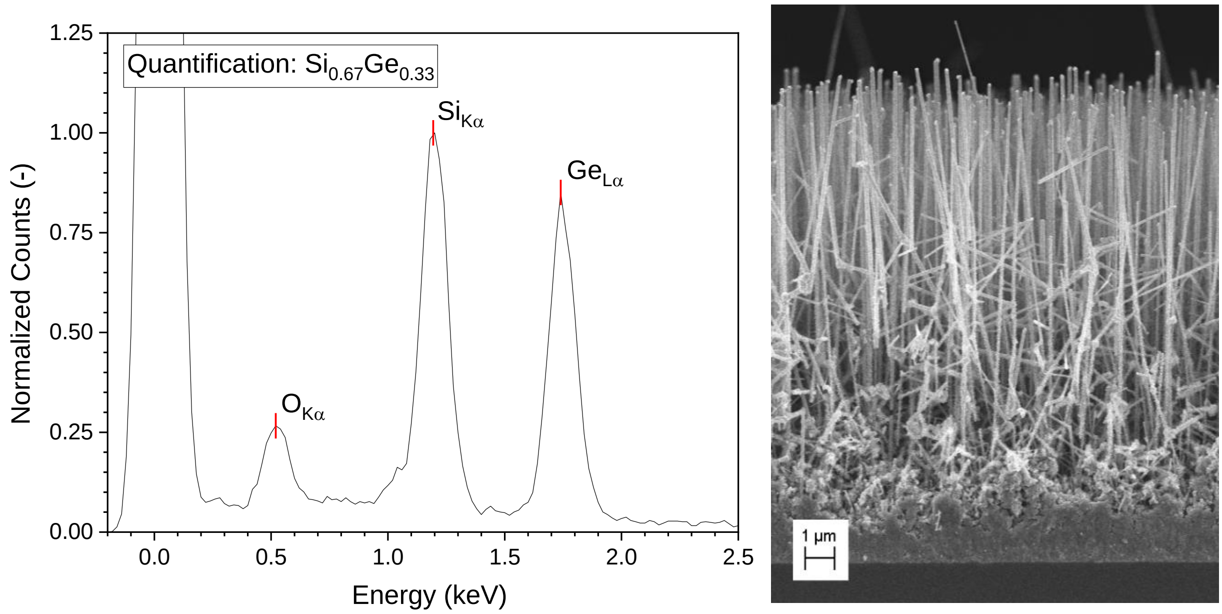

Supplementary Figure 11. A) EDS spectrum used for the compositional analysis of the SiGe NW. B) Cross sectional view of a Si chip with SiGe NWs grown in the same VLS process as the studied NW.

7. Additional z scan data

As it is summarized in section 4.4, additional κ estimations were performed using the detachment curves of the z scans. Supplementary Figure 12 shows the δG curve as a function of the tip position for the Si NW whereas results of the SiGe NW are shown in Supplementary Figure 13.

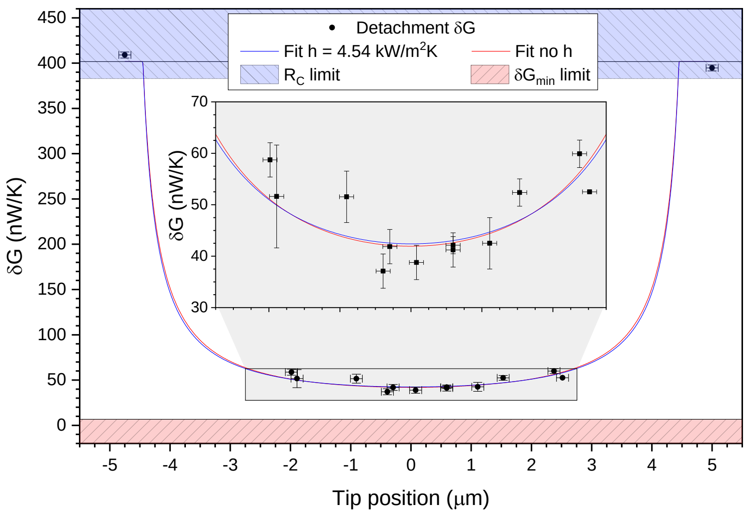

Supplementary Figure 12. Contact conductance change as a function of tip position for the detachment scans over the Si NW.

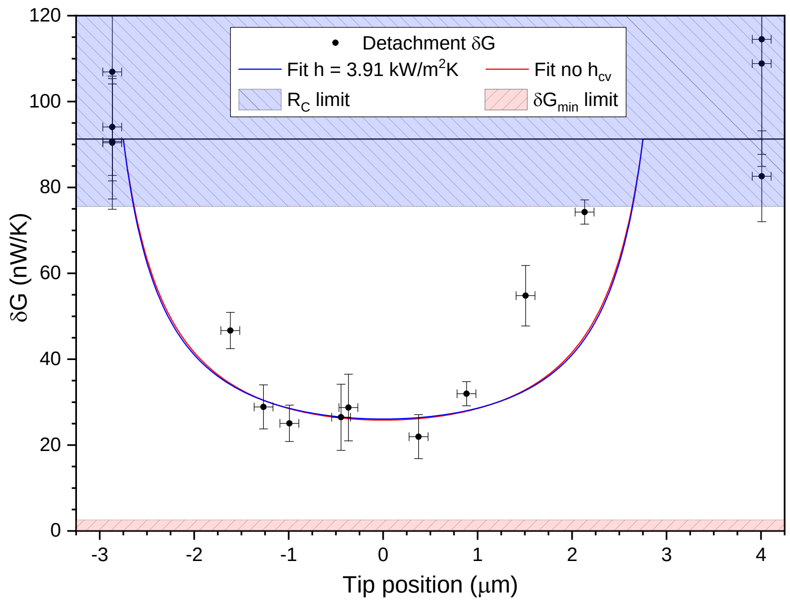

Supplementary Figure 13. Contact conductance change as a function of tip position for the detachment scans over the SiGe NW.

As it was remarked in Table 3 of the main article, slightly different values of κ were obtained depending on the set of data used. While some variation can be attributed to the stochastic noise of the measurement (especially relevant in the case of the rough surface of Si NWs) a second consideration perhaps more relevant has to be considered. If the force curves of a single point z-approach measurements are plotted (Supplementary Figure 14) one can see that the attachment and detachment points do not fully coincide. This difference is due to the attractive forces taking place in the contact. In the approach case the tip needs to reach lower to the NW until the event takes place. When the tip is already in contact, G dependence with z is considerably less relevant as the NW presents an alternative path thermal path, thus the G curve is flattened considerably (se Figure 1D and Supplementary Figure 3).

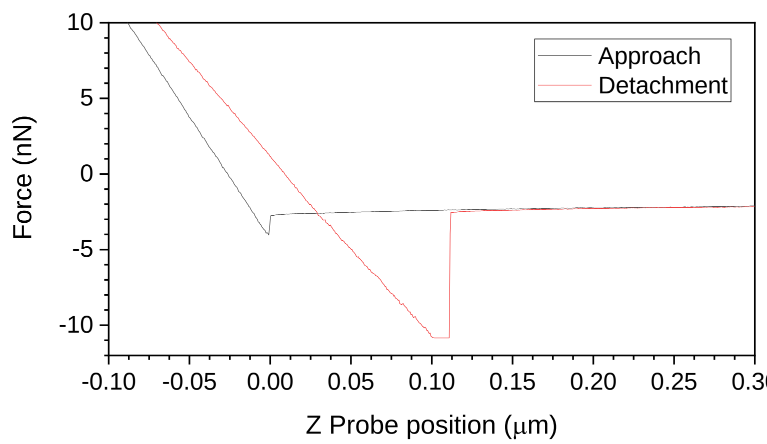

Supplementary Figure 14. Comparison between approach and detachment force curves. The sticking forces between tip a nanostructure hold the union for at least 100 nm above the NW rest height until the detachment event took place (when elastic forces of the NW overcome them). The flatness in the detachment curve was produced by and out-of-scale event.

In the detachment scan, the NW is stick to the tip and it can be bended upwards a few nm from the horizontal equilibrium height until the electric forces are enough to detach the NW from the tip. When this happens, the SThM tip is higher than when the contact took place. As the G measured is also strongly dependent of the tip height, the measured δG might seem bigger because it is attributing to the δG a z variation of G. Thus, a higher κ might be inferred due to this artefact likely making this hysteresis-like effect responsible for the differences in values obtained.

Bibliography:

[1] Park Systems, Scanning Thermal Microscopy for XE Series SPM - Operation Manual, (n.d.). https://parksystems.com/park-spm-modes/thermal-properties/252- scanning-thermal-microscopy-sthm (accessed July 25, 2020).

[2] W. Chen, Y. Feng, L. Qiu, X. Zhang, Scanning thermal microscopy method for thermal conductivity measurement of a single SiO2 nanoparticle, Int. J. Heat Mass Transf. 154 (2020). https://doi.org/10.1016/j.ijheatmasstransfer.2020.119750.

[3] A. Assy, S. Lefèvre, P.O. Chapuis, S. Gomès, Analysis of heat transfer in the water meniscus at the tip-sample contact in scanning thermal microscopy, J. Phys. D. Appl. Phys. 47 (2014) 1–5. https://doi.org/10.1088/0022-3727/47/44/442001.

[4] A. Assy, S. Gomès, Temperature-dependent capillary forces at nano-contacts for estimating the heat conduction through a water meniscus, Nanotechnology. 26 (2015) 355401. https://doi.org/10.1088/0957-4484/26/35/355401.

[5] A. Giri, P.E. Hopkins, Analytical model for thermal boundary conductance and equilibrium thermal accommodation coefficient at solid/gas interfaces, J. Chem. Phys. 144 (2016). https://doi.org/10.1063/1.4942432.

[6] E. Dimaggio, G. Pennelli, Potentialities of silicon nanowire forests for thermoelectric generation, Nanotechnology. 29 (2018) 135401. https://doi.org/10.1088/1361-6528/aaa9a2.

[7] S. Elyamny, E. Dimaggio, S. Magagna, D. Narducci, G. Pennelli, High Power Thermoelectric Generator Based on Vertical Silicon Nanowires, Nano Lett. 20 (2020) 4748–4753. https://doi.org/10.1021/acs.nanolett.0c00227.

[8] B. Xu, K. Fobelets, Spin-on-doping for output power improvement of silicon nanowire array based thermoelectric power generators, J. Appl. Phys. 115 (2014) 214306. https://doi.org/10.1063/1.4881781.

[9] P. Ferrando-Villalba, L. D'Ortenzi, G.G. Dalkiranis, E. Cara, A.F. Lopeandía, L. Abad, R. Rurali, X. Cartoixà, N. De Leo, Z. Saghi, M. Jacob, N. Gambacorti, L. Boarino, J. Rodríguez-Viejo, Impact of pore anisotropy on the thermal conductivity of porous Si nanowires, Sci. Rep. 8 (2018) 12796. https://doi.org/10.1038/s41598-018-30223-0.

[10] O. Vazquez-Mena, G. Villanueva, V. Savu, K. Sidler, M.A.F. van den Boogaart, J. Brugger, Metallic Nanowires by Full Wafer Stencil Lithography, Nano Lett. 8 (2008) 3675–3682. https://doi.org/10.1021/nl801778t.

[11] A. Koumela, D. Mercier, C. Dupré, G. Jourdan, C. Marcoux, E. Ollier, S.T. Purcell, L. Duraffourg, Piezoresistance of top-down suspended Si nanowires, Nanotechnology. 22 (2011). https://doi.org/10.1088/0957-4484/22/39/395701.

[12] R. Juhasz, N. Elfström, J. Linnros, Controlled fabrication of silicon nanowires by electron beam lithography and electrochemical size reduction, Nano Lett. 5 (2005) 275–280. https://doi.org/10.1021/nl0481573.

[13] G. Pennelli, Top down fabrication of long silicon nanowire devices by means of lateral oxidation, Microelectron. Eng. 86 (2009) 2139–2143. https://doi.org/10.1016/j.mee.2009.02.032.

[14] G. Nellis, S. Klein, Heat Transfer, 1st ed., Cambridge University Press, Wisconsin, 2009.

[15] S.G. Jennings, The mean free path in air, J. Aerosol Sci. 19 (1988) 159–166.

https://doi.org/10.1016/0021-8502(88)90219-4.

[16] G. Chen, Nanoscale Energy Transport and Conversion: A Parallel Treatment of Electrons, Molecules, Phonons and Photons, Oxford University Press, Oxford, U.K., 2005.

[17] H.-D. Wang, J.-H. Liu, X. Zhang, T.-Y. Li, R.-F. Zhang, F. Wei, Heat Transfer between an Individual Carbon Nanotube and Gas Environment in a Wide Knudsen Number Regime, J. Nanomater. 2013 (2013) 1–7. https://doi.org/10.1155/2013/181543.

[18] J. Gao, D. Xie, Y. Xiong, Y. Yue, Thermal characterization of microscale heat convection in rare-gas environment by a steady-state “hot wire” method, Appl. Phys. Express. 11 (2018) 066601. https://doi.org/10.7567/APEX.11.066601.

[19] A. Bondi, Van der waals volumes and radii, J. Phys. Chem. 68 (1964) 441–451. https://doi.org/10.1021/j100785a001.

[20] W.M. Trott, J.N. Castaeda, J.R. Torczynski, M.A. Gallis, D.J. Rader, An experimental assembly for precise measurement of thermal accommodation coefficients, Rev. Sci. Instrum. 82 (2011). https://doi.org/10.1063/1.3571269.